Earth and Planetary Science Letters 607 (2023) 118066

Contents lists available at ScienceDirect

Earth and Planetary Science Letters

journal homepage: www.elsevier.com/locate/epsl

Relative sea level response to mixed carbonate-siliciclastic sediment loading along the Great Barrier Reef margin

Yucheng Lin [a,*], Pippa L. Whitehouse [a], Fiona D. Hibbert [b], Sarah A. Woodroffe [a], Gustavo Hinestrosa [c], Jody M. Webster [c]

[a] Department of Geography, Durham University, Durham, DH1 3LE, UK
[b] Department of Environment and Geography, University of York, York, YO10 5NG, UK
[c] Geocoastal Research Group, School of Geosciences, The University of Sydney, NSW 2006, Australia

ARTICLE INFO

Article history:
Received 1 July 2022
Received in revised form 10 February 2023
Accepted 15 February 2023
Available online 1 March 2023
Editor: Y. Asmerom

Keywords:
the Great Barrier Reef
sediment isostatic adjustment
glacial isostatic adjustment
sea-level change
sediment evolution
statistical inversion

ABSTRACT

The continental shelf along northeastern Australia is the world's largest mixed carbonate-siliciclastic passive margin and the location of the Great Barrier Reef (GBR). Following sea-level transgression during the last deglaciation, extensive sediment was deposited along the GBR due to neritic carbonate deposition (including shelf edge reefs, Holocene reefs and *Halimeda* bioherms) and fluvial discharge of terrigenous siliciclastic sediments. Such sediment loading can alter local relative sea level (RSL) by several metres through the sediment isostatic adjustment (SIA) process, a signal that is poorly constrained at the GBR. In this study, we used a glacial isostatic adjustment (GIA) model to develop an ensemble-based sediment loading history for the GBR since Marine Isotope Stage 2 (MIS 2). A Bayesian style framework is adopted to calibrate the sediment history ensemble and GIA model parameters using a sea-level database. According to our results, 1853.7 Gt (1613.1-2078.7 Gt, 95% confidence interval) of sediment have been deposited across the GBR since MIS 2 (28 ka BP), causing spatially variable relative sea-level change with the highest magnitude (0.9-1.1 m) found in the outer shelf of the southern central GBR (18.4-21.6° S). Because the SIA-induced RSL rise is unrelated to ice mass loss, failing to correct for this signal will lead to systematic overestimation of grounded ice volume by up to $\sim 4.3 \times 10^5$ km^3 during the Last Glacial Maximum. Additionally, we found that spatial variation in sediment loading and coastal environment may explain the different RSL history documented by published fossil coral reef records from Noggin Pass and Hydrographer's Passage. These results highlight the importance of considering SIA for any postglacial sea-level studies adjacent to large sediment systems. Lastly, by quantifying both the GIA and SIA signals, we provide a spatially and temporally complete RSL reconstruction that is well-suited to be used as a boundary condition to study the evolution of the GBR shelf and slope sedimentary system.

1. Introduction

Located on the world's largest mixed carbonate-siliciclastic passive margin in northeastern Australia, the Great Barrier Reef (GBR) is an ideal place to study coral reef framework development and terrigenous sediment transportation in response to sea-level variation during glacial cycles (Webster et al., 2018). To accurately understand and model the physical and ecological mechanisms behind the spatio-temporal evolution of this complex sediment system, a key boundary condition is the relative sea-level (RSL) change history, which is by far the most important driver on millennial timescales (Hopley et al., 2007; Woodroffe and Webster, 2014). Previous work suggests strong spatial variability in past RSL along this >2000 km coastline (Lambeck et al., 2002), prompting the need for a comprehensive understanding of the processes controlling sea-level change in this region. Currently, the most commonly-used physical model to explain this variability is a glacial isostatic adjustment (GIA) model, which describes the solid Earth and ocean surface response to changes in surface loading due to ice-ocean mass redistribution. Based on GIA theory, RSL recorded at the far-field location (i.e., far from previous ice sheet margins) of the GBR is primarily a function of solid Earth rheology, the change in global ice volume through time and local shelf morphology (Lambeck et al., 2014), with these factors

* Corresponding author.
E-mail address: yucheng.lin@durham.ac.uk (Y. Lin).

https://doi.org/10.1016/j.epsl.2023.118066

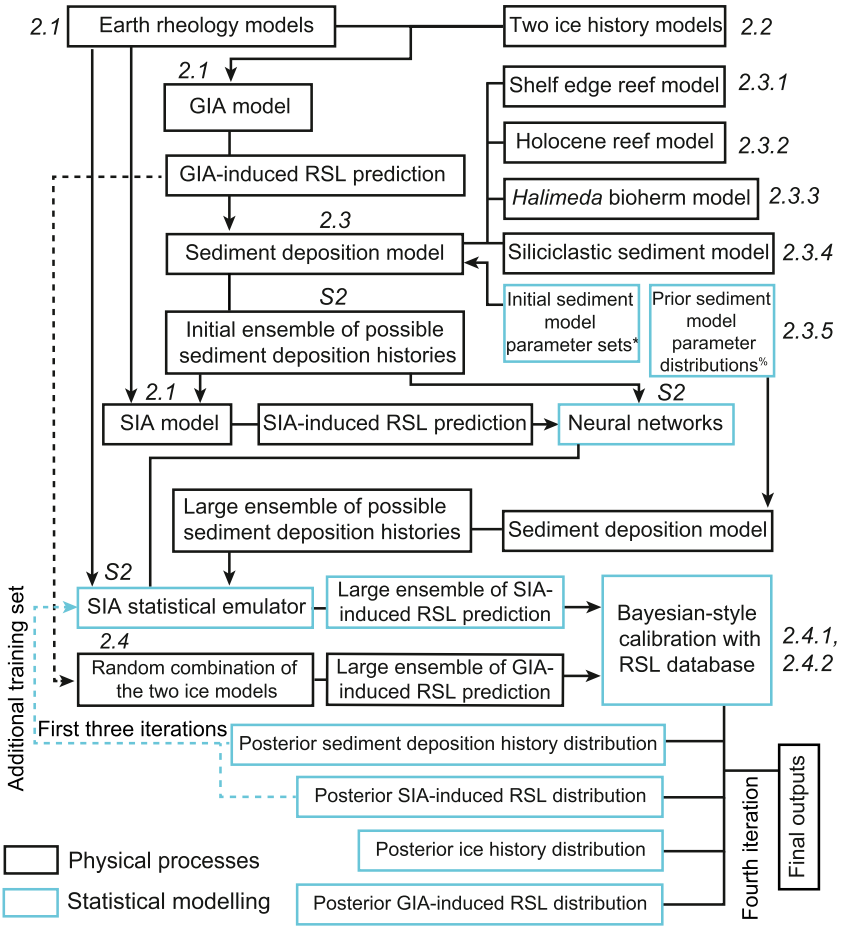

Fig. 1. Schematic overview of the inversion procedure adopted in this study. The black and blue boxes represent the physical processes and statistical modelling processes and results, respectively. Each arrow indicates that a previous model output acts as the input for the next model. *Initial sediment model parameter sets denote six sediment parameter combinations used to generate sediment models to train a SIA statistical emulator (details in Supplementary section 2). %Prior sediment model parameter distributions are given in Table 1, which can be used to create a large ensemble of random sediment models. Note the sediment deposition model appears in multiple places. The annotated italic number beside each box indicates the section that provides detailed descriptions of each modelling procedure, S2 indicates Supplementary section 2.

having previously been invoked to explain different magnitudes of postglacial RSL rise (Yokoyama et al., 2006) and mid-Holocene highstand (Lambeck et al., 2002) along the GBR coastline.

However, recent coral reef records from Noggin Pass (NOG) and Hydrographer's Passage (HYD), two shelf edge sites with similar shelf morphology located 500 km apart from each other, show a consistent RSL offset (reconstructed RSL at NOG is several metres higher at HYD) during the last deglaciation (Yokoyama et al., 2018; Webster et al., 2018) which cannot be explained by a GIA model. To understand this discrepancy, an additional physical process that is able to generate metre scale regional RSL variation within a 10^3-10^5 year timescale is required. For coral reef records from a passive margin, minimally impacted by sediment compaction, the most obvious possibility is RSL change caused by sediment loading (Horton et al., 2018). Similar to ice loading, sediment loading can lead to isostatic adjustment that changes the local geoid and deforms the land surface depending on the regional load magnitude and Earth rheology (i.e., sediment isostatic adjustment, SIA; Dalca et al., 2013). Previous studies suggest there have been more than 1000 gigaton (Gt) of neritic carbonate sediment (Hinestrosa et al., 2022; Rees, 2005) accumulated across the GBR since the Last Glacial Maximum (LGM) along with a considerable amount of fluvial discharge of terrigenous siliciclastic sediment (Salles et al., 2018). Such sediment loading could be large enough to drive localised RSL variations.

In this study, we aim to simultaneously quantify the ice, ocean and sediment loading impact on RSL variation across the GBR from Marine Isotope Stage (MIS) 2 to present. To quantify the SIA signal, we develop a GIA-model-enabled ensemble-based sediment accretion model, which allows us to reconstruct the spatio-temporal evolution of sediment deposition across the GBR. We then use a Bayesian formalism to calibrate the net RSL history predicted by the GIA and SIA models using a sea-level database. The outputs of our study are a set of high-quality predictions of RSL change and sediment deposition history, with quantified uncertainty (Fig. 1).

2. Methodology

The methodology for reconstructing RSL change across the GBR is comprised of three major components: GIA/SIA modelling, sediment deposition history reconstruction and statistical calibration of the first two components using a GBR sea-level database (Fig. 1).

2.1. Glacial/sediment isostatic adjustment modelling

In this study, we describe RSL variation as a combined signal caused by GIA and SIA (Wolstencroft et al., 2014). We compute GIA-induced RSL change using a gravitationally self-consistent theory that accounts for migrating shorelines and Earth rotational feedback (Kendall et al., 2005; Mitrovica et al., 2005). For SIA,

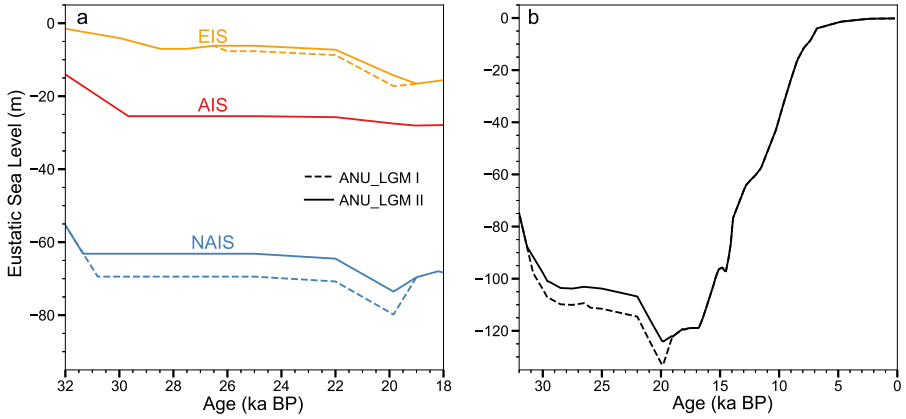

Fig. 2. Ice history modifications. (a) Pre-LGM ice history modifications for three ice sheets. (b) Modified global ice histories. The dashed and solid lines indicate the scenarios I and II we tested in this study. Note we use the same Antarctic model for both ice loading scenarios. NAIS = North American Ice Sheet; AIS = Antarctic Ice Sheet; EIS = Eurasian Ice Sheet.

we use the methodology of Wolstencroft et al. (2014) which considers the RSL change caused by sediment-driven Earth deformation without considering the sediment impact on geoid variation, shoreline migration and Earth rotation as they are minor signals (generally accounting for less than 5% of the total SIA caused RSL signal; Ferrier et al., 2018). Although a self-consistent GIA and SIA model has recently been developed (Ferrier et al., 2017), we do not adopt this model here because we wish to rigorously sample the GBR deposition sediment history uncertainty range independently, and solving for the gravitationally self-consistent response to both ice and sediment loading would significantly increase the required computational power.

The Earth model used in this study is represented by a spherically symmetric Maxwell body consisting of an elastic lithosphere, and an upper and lower mantle extending to 670 km and from 670 km to the core-mantle boundary, respectively. The elastic and density structure of the Earth model is derived from the preliminary reference Earth model (Dziewonski and Anderson, 1981). To sample the uncertainty range associated with the rheological properties of the Earth we test lithospheric thickness values of 46, 71 and 96 km and upper and lower mantle viscosity values ranging between 0.05-1 and 1-90 $\times$ 10^{21} Pa s, respectively. The relatively thin lithosphere and weak upper mantle viscosity values that we explore reflect the values constrained by previous GIA studies of the GBR region (Ishiwa et al., 2019; Lambeck et al., 2002) and are supported by a recent global 3D mantle viscosity reconstruction (Austermann et al., 2021). In total, we test 228 Earth model combinations. We use the same Earth model for calculating GIA and SIA in order to produce internally consistent RSL predictions. We perform all calculations using a spherical harmonic truncation of degree and order 512 ($\sim$40 km), which is suitable for calculating long-wavelength SIA and GIA signals in regions where lithospheric thickness is $\sim$50 km or greater, such as the GBR.

2.2. Ice model

We use a version of the ANU ice model (denoted as ANU_LGM; Lin, 2019) that has been updated to reflect the early rapid global mean sea-level (GMSL) fall to the LGM lowstand, as revealed by sea-level index points (SLIPs) from NOG and HYD (Yokoyama et al., 2018; Webster et al., 2018). We assume that the majority (90%) of this GMSL fall was caused by rapid growth of the North American and Eurasian Ice Sheets (Fig. 2), possibly due to the saddle merger mechanism (Ji et al., 2021). Because GMSL prior to the LGM is poorly-constrained, we test two possible ice loading scenarios, corresponding to a 134 m (scenario I; Lambeck et al., 2014) and a 125 m (scenario II; Yokoyama et al., 2018) GMSL lowstand, which can considered as two end-member scenarios of the LGM GMSL lowstand.

2.3. Sediment model

To reconstruct a complete sediment history for the GBR, we divide its sediment system into four domains: shelf edge reef, Holocene reef, *Halimeda* bioherms (the first three are carbonate sediment) and siliciclastic sediment (Fig. 3). We then use 456 GIA-induced RSL histories (produced by combining 2 ice models with 228 Earth models) to force simple linear accretion models and reconstruct the sediment history for each domain as an ensemble (Fig. 1). Sediment accretion is first reconstructed at high spatial resolution by combining the RSL predictions with a 100 m resolution modern GBR digital elevation model (DEM, Beaman, 2010) to create a series of palaeo-DEMs, and hence determine the detailed spatial evolution of inundation and sediment accretion. For the purposes of calculating the SIA response, net sediment load in each $\sim$40 km grid cell of our study region is then summed to produce a loading time series. We do not consider the influence of hydrodynamic effects on sediment distribution because short-wavelength variations in surface load will have a relatively minor effect on the SIA signal, which is long-wavelength and is spatially and temporally smooth.

2.3.1. Shelf edge reef

The shelf edge is defined as the region between the modern outer barrier reef front and the 130 m isobath (Fig. 3, Beaman, 2010; Abbey et al., 2011). Based on the evidence derived from drill cores at NOG and HYD, the shelf edge reef growth structure can be described by four reef formation-demise sequences: reef 2 (27-22 ka BP; initiation and demise time), reef 3a (22-17 ka BP), reef 3b (17-14 ka BP) and reef 4 (14-10 ka BP; modified from Webster et al., 2018).

To reconstruct the spatio-temporal reef development, we adopt a linear accretion model from Hinestrosa et al. (2022). For this model, the averaged vertical accretion rate (ν_{se}) and maximum accretion thickness (τ_{se}) are defined for each reef sequence based on the dating of drill core material from HYD and NOG (Supplementary Figure 1). We assume each reef sequence initiates after local inundation, with a time lag (ι_{se}) of between 0 and 1 ka, and that it accumulates uniformly following the rate of ν_{se} until reaching thickness τ_{se}. The 0-1 ka lag between local inundation and reef initiation is defined based on observational evidence from Sanborn et al. (2020). Each reef within the shelf edge polygon (i.e., each DEM

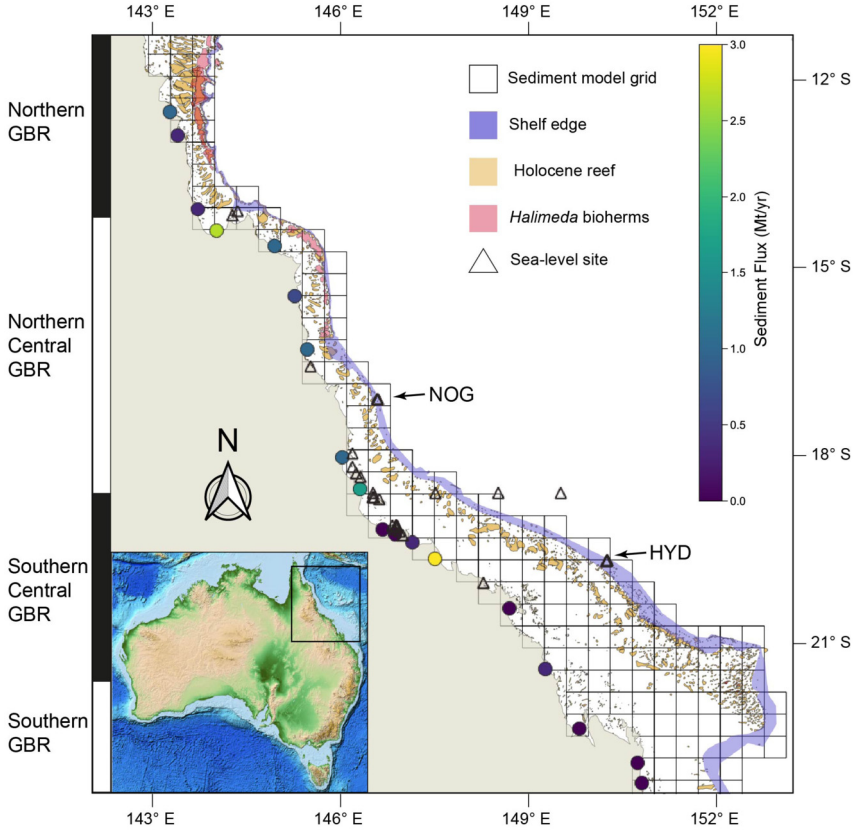

Fig. 3. Overview of four sediment domains. The orange polygons indicate the locations where Holocene reefs accumulate. The purple polygons outline the domains where shelf edge reefs are likely to have accumulated (shelf edge reefs have not yet been fully mapped along the GBR margin). In the northern GBR, pink polygons show the locations of *Halimeda* bioherms. Coloured dots along the modern coastline indicate the rate of present-day fluvial sediment discharge (Milliman and Farnsworth, 2013). The black triangles are the RSL site locations used to calibrate the sediment loading history. The zebra boxes on the left indicate the four latitudinal GBR regions defined in 2.3.5. The sediment loading grid is indicated by the black squares.

grid cell) is classified to one of the four reef sequences (Webster et al., 2018) based on its initiation time, which in turn determines its ν_{se} and τ_{se}. Because constraints on ν_{se} and τ_{se} are currently only available for HYD and NOG, we assume the information derived from them is representative of the southern and northern GBR, respectively.

2.3.2. Holocene reef

The spatial distribution of the Holocene reef has been mapped by modern bathymetric and remote sensing surveys (http://www.gbrmpa.gov.au/). The only variable to estimate is the spatially-variable Holocene reef accretion thickness, which will vary according to local environmental conditions (Hinestrosa et al., 2022; Hopley et al., 2007). To account for this heterogeneity, we use a kriging method (details in supplementary section 1) to interpolate the spatial pattern of reef accretion thickness based on a Holocene reef accretion thickness database (Hinestrosa et al., 2022, Supplementary Figure 2). One advantage of this method is that the uncertainty estimation is included in its conceptualisation, hence the interpolation uncertainty can be easily propagated.

Next, to accurately determine the time when the local pre-Holocene substrate was flooded, we create a pre-Holocene GBR DEM by subtracting the interpolated accretion thickness from the modern DEM. We carry out calculations based on this pre-Holocene DEM. We then combine our 456 GIA-induced RSL predictions with this pre-Holocene DEM to create a series of palaeo-DEMs that can be used to determine the timing of local inundation and hence the temporal development of the Holocene reefs. Using interpolated reef accretion thickness estimates as a boundary condition, each Holocene reef is assumed to begin accumulating following local sea-level transgression, with a time lag (ι_{ho}) of between 0 and 1 ka (same as shelf edge reef), and stop accumulating when local RSL is 30 m higher than the modern reef surface (i.e., when the coral reef surface becomes too deep for significant shallow water reef growth). Where the modern water depth is less than 30 m, we assume the reef stops accumulating when local RSL first reaches its maximum value (mid-Holocene highstand or present). Between the defined starting and terminating time, reefs are assumed to grow at a linear rate depending on the interpolated accretion thickness.

2.3.3. Halimeda bioherms

Halimeda bioherms are a dominant source of inter-reef carbonate deposits for the northern GBR and have been extensively mapped (Fig. 3, McNeil et al., 2016). McNeil et al. (2020) provide an overall estimate of 55.12 Gt of accumulation, corresponding to a 7.63 m sediment layer across all mapped regions of *Halimeda* bioherms (assumes aragonite density of 2.94 g/m^2 with 0.58 porosity (McNeil et al., 2020)). As for the Holocene reef sediment model, we build a pre-Holocene DEM for the *Halimeda* bioherms domain by subtracting 7.63 m from the original GBR DEM within the accumulation region (i.e., pink polygons in Fig. 3). The temporal evolution of the *Halimida* bioherms is then calculated using the same method as for the Holocene reef model, using a lag parameter ι_{ha}. Although previous studies suggest that other sources of carbonate sediment accumulate across inter-reef regions, such as benthic foraminifera and coralline algae (Hopley et al., 2007), at present there is no comprehensive database which documents the inter-reef carbonate thickness or mass accumulation since MIS 2. We

therefore do not consider this possible source of carbonate sediment in our reconstruction.

2.3.4. Siliciclastic sediment

To quantify siliciclastic load, we use a modern global database of fluvial sediment flux measurements (Fig. 3, Milliman and Farnsworth, 2013) and assume the averaged discharge rate for the whole of the deglacial period is proportional to the modern measurement, with absolute values controlled by a scaling parameter (β) that increases/decreases the modern sediment flux by up to 40%. For each model run, the sediment discharge rate is assumed to be temporally constant. The spatial distribution of siliciclastic sediment deposition will have varied through time due to shoreline migration during postglacial sea-level change. This palaeo shoreline migration is reconstructed by combining a modern DEM with GIA-induced RSL predictions. For each model time step, sediment load is discharged to the nearest palaeo shoreline location relative to the modern river mouth position (Fig. 3). To conserve mass, we uniformly remove a layer of sediment from the North East Coast drainage basin with a mass equivalent to the siliciclastic sediment deposition in the ocean.

2.3.5. Sediment model parameters

We use two types of parameter (pattern and magnitude) to represent uncertainties in the sediment history reconstructions. For all sediment domains, Earth and ice model parameters are the primary pattern parameters because they determine the spatio-temporal pattern of RSL variation, and in turn the sediment accumulation pattern. Additionally, the lag parameters mentioned above (ι_{se}, ι_{ho}, ι_{ha}) allow a delay to the initiation of carbonate sediment accumulation of between 0 and 1 ka after local transgression, which provides additional control on the temporal evolution of the three carbonate sediment domains.

The magnitude parameters control the magnitude of sediment accumulation for each domain. When determining the sediment accretion thickness of the shelf edge reef, we limit the maximum reef accretion thickness for the four reef sequences using the parameters $\tau_{2,3a,3b,4}$ (Table 1, values are empirically derived from Hinestrosa et al., 2022). For the Holocene reef, the accretion thickness is subject to spatially variable uncertainty produced by the kriging interpolation, which is described by $\alpha_{ho}(\varphi)$, and varies from -3σ to 3σ. Lastly, the magnitude of the siliciclastic sediment load is controlled by a scaling parameter β (section 2.3.4).

The reconstructed sediment accumulation thickness $H(\varphi, t)$ at location φ and time t is converted to a sediment load, $M(\varphi, t)$, by:

$$M_{se}(\varphi, t) = H_{se}(\varphi, t)A(\varphi)\rho_a(1 - \phi_{se})\epsilon_{se} \quad (1)$$

$$M_{ho}(\varphi, t) = H_{ho}(\varphi, t)A(\varphi)\rho_a(1 - \phi_{ho})\alpha_{ho}(\varphi) \quad (2)$$

$$M_{hb}(\varphi, t) = H_{hb}(\varphi, t)A(\varphi)\rho_a(1 - \phi_{hb}) \quad (3)$$

where fixed parameters $A(\varphi)$ and ρ_a indicate bathymetric grid cell area and the density of aragonite (2.94 g/cm^3). ϕ is the averaged sediment porosity for the shelf edge (se), Holocene (ho) and *Halimeda* bioherms (hb) domains; it is allowed to vary from 25% to 45% to represent uncertainty of the overall accumulation magnitude. For the shelf edge reef, one important uncertainty is that only a minor part of our defined shelf edge area (Fig. 3) is covered by reefal deposit, i.e., significantly thicker sediment than the surrounding area. Therefore, we assign a reefal area percentage parameter (ϵ_{se}), varying between 10-30% (derived from seismic mapping of shelf edge reef structure, Hinestrosa et al., 2016), to describe this uncertainty. Although the non-reefal area shows substantially lower sediment thickness (generally <10 m, Hinestrosa et al., 2016), it covers a much larger proportion of the shelf edge area, meaning it can potentially contribute as much sediment loading as the reefal area. Therefore, the upper limit of ϵ_{se} is doubled (to 60%) to account for this condition. To reduce computation time, we combine $1 - \phi_{se}$ and ϵ_{se} in the shelf edge reef model (as γ_{se}), and $1 - \phi_{ho}$ and $\alpha_{ho}(\varphi)$ in the Holocene reef model (as γ_{ho}) together, as they are all scaling parameters.

Due to different climate, local antecedent substrate and shelf physiography, previous studies suggest a contrasting sediment deposition system between the northern and southern GBR (Hinestrosa et al., 2016). Considering this difference, we separate the whole GBR region into northern (10-14.2° S, Fig. 3), northern-central (14.2-18.4° S), southern-central (18.4-21.6° S) and southern GBR (21.6-26.2° S) sectors based on the definition from Hinestrosa et al. (2019). All sediment parameters are allowed to vary between sectors (Table 1), which is indicated by the superscripts 1 (northern), 2 (northern central), 3 (southern central) and 4 (southern). We use the same prior distributions for sediment model parameters across all four regions, except the thickness parameters $\tau_{2,3a,3b,4}$; our compiled database generally shows thicker sediment in the southern GBR (HYD) compared to the north (NOG, Supplementary Figure 1) so we use different prior distributions for these parameters in each region. The prior distributions for all sediment domain parameters are given in Table 1 and the resulting sediment loading history prior distributions are given in Supplementary Figure 4.

2.4. Statistical calibration

During the calibration process, to consider uncertainty associated with the poorly-constrained pre-LGM ice history, we allow the ice model to vary between scenarios I and II using a weighting parameter ω. The final RSL predictions are calculated using a weighted combination of the two ice history scenarios. ω therefore indicates the data preference for the assumed pre-LGM ice history. The data used for calibration are sea-level index points (SLIPs). Each SLIP provides information about the age and height of past RSL at a single location, which is assumed to represent the combined signal of GIA and SIA processes. Based on SLIP databases, we use a Bayesian framework to sample the posterior probability density distribution for each model parameter (Table 1) conditioned on sea-level data (Fig. 1).

2.4.1. Calibration data

We compile a GBR RSL database following the methodology of Hibbert et al. (2018, 2016). For radiocarbon dated SLIPs we recalibrate the conventional radiocarbon age using the SHCal20 calibration curve (Hogg et al., 2020) for terrestrial samples, and Marine20 (Heaton et al., 2020) with appropriate and up-to-date local marine reservoir corrections (ΔR; http://calib.org/marine) for marine samples. For Uranium-Thorium dated coral samples we recalculate the U-series ages where necessary, assuming a closed system with the latest decay constant (Cheng et al., 2013). We only include the U-series ages that pass the age reliability screening criteria of [^{232}Th] $\leq$ 2 ppb and $\delta^{234}U_{initial}$ = 147 $\pm$ 5‰. We exclude any SLIPs that are explicitly stated as not being *in situ* by the original paper.

For SLIP depth uncertainty we use local palaeo-water depth determination for each record taken from original publications, assuming that the indicator may occur equally anywhere within the given upper and lower limit (i.e., the uniform distribution scenario, Hibbert et al., 2016, 2018; Lin et al., 2021). Additionally, we consider the elevation measurement uncertainty caused by coring, levelling and tectonic correction when necessary. Overall, our study uses 375 SLIPs (supplementary database). To systematically quantify the RSL difference between NOG and HYD, we use a Monte Carlo binning analysis approach to reconstruct the underlying RSL signal at these two sites. The details of this approach are given in Supplementary section 3.

Table 1
Table of prior sediment model parameters. We assume a uniform prior distribution for all parameters within the defined parameter space. The uniform distributions with parentheses indicate a continuous uniform distribution, those with square brackets indicate a discrete uniform distribution comprising the listed parameters. Superscripts 1 to 4 represent spatially different parameters for the northern, northern central, southern central and southern GBR.

Model Component	Parameters and Prior Distribution(s)	Parameter Description
Earth model	LT $\sim U$[46,71,96]	Effective lithospheric thickness with unit kilometre
	μ_{up} $\sim U$[0.05,0.08,0.1,0.2,0.3,0.5,0.8,1]	Upper mantle viscosity with unit 10^{21} Pa s
	μ_{lo} $\sim U$[1,2,3,5,8,10,20,30,50,70,90]	Lower mantle viscosity with unit 10^{21} Pa s
Ice model	ω $\sim U(0,1)$	Relative weighting associated with ice loading scenario II
Shelf edge reef	γ_{se}^{1-4} $\sim U(0.055,0.45)$	A combined parameter that describes the uncertainty associated with shelf edge reef formation porosity and reefal area percentage
	τ_2^{1-4} $\sim U(5,10)$, $U(5,10)$,$U(5,15)$,$U(5,15)$	Maximum accretion thickness for shelf edge reef stage 2 with unit metre (same for all maximum accretion thickness parameters below)
	τ_{3a}^{1-4} $\sim U(10,20)$,$U(10,20)$,$U(15,30)$,$U(15,30)$	Maximum accretion thickness for shelf edge reef stage 3a
	τ_{3b}^{1-4} $\sim U(5,15)$,$U(5,15)$,$U(10,20)$,$U(10,20)$	Maximum accretion thickness for shelf edge reef stage 3b
	τ_4^{1-4} $\sim U(5,15)$,$U(5,15)$,$U(10,20)$,$U(10,20)$	Maximum accretion thickness for shelf edge reef stage 4
	ι_{se}^{1-4} $\sim U$[0,0.2,0.4,0.6,0.8,1]	Lag between local inundation and shelf edge reef initiation with unit ka (same for all lag parameters below)
Holocene reef	γ_{ho}^{1-4} $\sim U(-3\sigma,3\sigma)$	A combined parameter that describes the uncertainty associated with reef formation porosity and kriging determined reef depth uncertainty (defined by σ).
	ι_{ho}^{1-4} $\sim U$[0,0.2,0.4,0.6,0.8,1]	Lag between local inundation and Holocene reef initiation
Halimeda bioherms	ϕ_{ha}^{1-4} $\sim U(0.25,0.45)$	*Halimeda* bioherms formation porosity
	ι_{ha}^{1-4} $\sim U$[0,0.2,0.4,0.6,0.8,1]	Lag between local inundation and *Halimeda* bioherms initiation
Siliciclastic sediment	β^{1-4} $\sim U(0.6,1.4)$	Averaged siliciclastic discharge rate relative to present day

2.4.2. Calibration procedure

The posterior probability distributions are calculated using a simulated annealing algorithm (Kirkpatrick et al., 1983), a probability-based technique which shows good capacity to converge to the global minimum solution. Within a Bayesian framework, a likelihood function describes the joint probability of the observed data as a function of the model parameters. We assume a uniform prior distribution for all model parameters (Table 1), meaning the posterior probability is equivalent to the likelihood. In this study we express the likelihood as:

$$p(y|x) = exp(-\frac{1}{N}\sum_{n=1}^{N} w_n J_n) \tag{4}$$

$$J_n = \sqrt{\frac{(RSL_n^y - RSL_n^m)^2}{\sigma_{RSL,n}^2} + \frac{(t_n^y - t_n^m)^2}{\sigma_{t,n}^2}} \tag{5}$$

where x is the vector of all model parameters, y is the SLIP data set consisting of n samples, each containing information about palaeo RSL height (RSL_n^y) and age (t_n^y) with 1 sigma uncertainties of $\sigma_{RSL,n}$ and $\sigma_{t,n}$, respectively. w_n is a weighting parameter to offset calibration bias due to variable temporal data density using the definition from Tarasov et al. (2012). For each set of model parameters, and for each SLIP location, a RSL curve is produced and we calculate the minimum distance (J_n) between the SLIP and the RSL curve, where RSL_n^m and t_n^m represent the RSL and age of the closest point on the modelled curve (adapted from Love et al., 2016). The minimum distance data-model comparison metric J provides a unitless measurement of model misfit for both chronological and vertical uncertainties. Because we assume past sea level may occur equally anywhere between the upper and lower limit of each SLIP, we assume no vertical misfit if the model predictions are within the 2 sigma uncertainty range of the observations. Therefore, we express RSL_n^y as:

$$RSL_n^y = \begin{cases} RSL_n^y + 2\sigma_{RSL,n}, & RSL_n^m \geq RSL_n^y + 2\sigma_{RSL,n} \\ RSL_n^m, & RSL_n^y - 2\sigma_{RSL,n} < RSL_n^m < RSL_n^y + 2\sigma_{RSL,n} \\ RSL_n^y - 2\sigma_{RSL,n}, & RSL_n^m \leq RSL_n^y - 2\sigma_{RSL,n} \end{cases} \tag{6}$$

Based on this likelihood formulization, we calculate the posterior probability distributions for each model parameter, and to speed up the calibration process, we use a statistical emulator to emulate the SIA process. Details on the implementation of this approach are provided in Supplementary section 2.

3. Results

Based on the posterior probability distributions of the model parameters drawn from the simulated annealing (Supplementary Table 1), we calculate the spatio-temporal field of sediment accumulation and RSL variation for the GBR. We start by presenting the results of the Earth and ice model parameter inversion and describe the resulting GIA-induced RSL predictions. Using these GIA predictions, we illustrate the palaeo GBR shoreline reconstructions and quantify how they affect the sediment accumulation history. Lastly, we present the sediment loading induced RSL change and RSL model-data comparison.

3.1. Earth and ice model parameters

The inversion results are given in Table 2. For a far-field region like the GBR, post-glacial sea-level change was predominantly driven by ice-ocean mass exchange (causing >100 m RSL change compared to ~1 m by SIA). Hence, although the Earth model parameters impact the prediction of both GIA- and SIA-induced RSL

Table 2
Inversion results. P_{max} indicates the value with the maximum posterior probability (i.e., best-fit value). The load values represent the total sediment load deposited during the last 28 ka BP, subscripts and superscripts are as follows: se = shelf edge reef; ho = Holocene reef, ha = *Halimeda* bioherms, si = siliciclastic discharge, 1= northern GBR, 2 = northern central GBR, 3 = southern central GBR, 4 = southern GBR.

	P_{max}	Expected Value	Standard Deviation	95% Confidence Interval
LT (km)	96	89.3	11.2	71-96
μ_{up} (10^{21} Pa s)	1	0.93	0.15	0.5-1
μ_{lo} (10^{21} Pa s)	30	38.3	11.3	20-50
ω	1	0.98	0.06	0.9-1
$Load_{total}$ (Gt)	1939.6	1853.7	112.4	1613.1-2078.7
$Load_{se}$ (Gt)	559.1	478.8	68.9	330.8-566.3
$Load_{ho}$ (Gt)	797.6	794.2	59.3	630.0-943.4
$Load_{ha}$ (Gt)	47.0	46.7	3.8	46.7-54.1
$Load_{si}$ (Gt)	536.3	534.0	61.3	410.5-659.1
$Load^1$ (Gt)	138.1	167.8	53.1	137.1-271.9
$Load^2$ (Gt)	183.1	229.8	59.3	169.3-361.0
$Load^3$ (Gt)	1007.2	994.6	45.7	905.0-1042.2
$Load^4$ (Gt)	611.3	461.5	98.9	296.2-617.5

change, the Earth model parameter distributions are primarily calibrated to replicate the GIA process. The maximum probability fit to the SLIPs is achieved using an Earth model combination of 96 km (71-96 km; 95% confidence interval, CI) lithospheric thickness, and 1 (0.5-1) and 30 (20-70) $\times$ 10^{21} Pa s upper and lower mantle viscosity. These inverted Earth parameters are generally consistent with recent global 3D viscosity field reconstructions (Austermann et al., 2021) but reflect a substantially stronger upper mantle compared with previous estimates based on GIA analysis of Holocene sea-level data from east Australia (0.15-0.3 $\times$ 10^{21} Pa s Lambeck et al., 2002). The main reason for this difference is our inclusion of pre-Holocene coral reef records, which prefer a stronger upper mantle viscosity (details in Supplementary Figure 6).

The ice model weighting parameter predominantly converges to scenario II (Fig. 2), indicating that a smaller pre-LGM grounded ice volume is preferred by the SLIPs. The blue dashed lines in Fig. 4 are the expected GIA-induced RSL change for RSL sites with at least five SLIPs; results for other RSL sites are shown in Supplementary Figure 8. It is clear that SLIPs with ages between 19.5 and 21.5 ka BP at NOG represent substantially higher RSL than the prediction produced by the preferred ice loading scenario II. Using scenario I, which has a larger LGM global ice volume, would result in an even lower RSL prediction during this period, therefore further enlarging the data-model misfit, leading to the rejection of this scenario in the inversion.

3.2. Sediment deposition history

3.2.1. Temporal distribution

Using the posterior Earth and ice model parameters, we show detailed palaeo shoreline positions (note that the SIA impact on shoreline migration is minor and is not considered here) for eight key time frames (Fig. 5). Comparing to the commonly used approach that assumes sea-level rise uniformly follows the GMSL curve (e.g., Hinestrosa et al., 2019), our calculation shows local RSL can significantly depart from GMSL by >10 m depending on local morphology. During early MIS 2 (28-22 ka BP; Fig. 2), RSL was 90-105 m below present with only part of the shelf edge submerged near the south-eastern Capricorn Channel. The growth of reef stage 2 here (Supplementary Figure 1; Webster et al., 2018) contributed 10% to overall sediment accumulation for this period (Fig. 6). Comparatively, 19.1 Gt/ka (14.7-23.5 Gt/ka) of siliciclastic sediment was deposited at the continental slope and shelf edge during this period, which dominated the sediment budget (contributing ~90% of total loading). This siliciclastic proportion became even greater when GMSL dropped to LGM conditions between 22-19.9 ka BP.

After the LGM, local sea level rose gradually prior to 16.5 ka BP and accelerated between 16.5 and 14.65 ka BP, which induced the coastline near the Capricorn Channel to migrate slightly onshore. As a result of the initiation of reef 3b and the continuous growth of reefs 3a and 2 (Supplementary Figure 1), shelf edge reef accumulation increased from 1.6 Gt/ka to 11.1 Gt/ka (Fig. 7b). Following the start of Meltwater Pulse 1A at 14.5 ka BP, the rate of local sea-level rise exceeded 40 m/ka, which further inundated the Capricorn Channel by hundreds of kilometres and caused the shelf edge accumulation rate to increase to ~20 Gt/ka. Although the RSL rise rate decreased to ~15 m/ka after 14.0 ka BP, the coastline continued to retreat significantly in the southern central GBR and less so in the northern central GBR until 13.2 ka BP. Due to the flat morphology of the southern central GBR shelf, a large area of middle shelf near Mackay was flooded at this time, initiating the growth of the Holocene reef. The rest of the outer-middle shelf within the southern central GBR was submerged following ~6.5 m RSL rise leading up to 12.6 ka BP. Meanwhile, north of the southern central GBR, most of the middle shelf and even parts of the shelf edge were still sub-aerially exposed, indicating the strong temporal variability in transgression time. The accretion rate of the shelf edge reef along the whole GBR continued to rise until 10 ka BP, when most of the shelf edge had been inundated with its contribution to the sediment budget peaking at 32.3% (Fig. 7c). Similarly, as the coastline moved across the middle shelf (except in the northern GBR), this accelerated the growth of the Holocene reef and initiated *Halimeda* bioherm growth at 11 ka BP. This timing agrees well with a recent radiocarbon analysis of inter-reef sediment cores, which suggests *Halimeda* bioherm initiation occurred around 11.1 ka BP in the northern GBR (McNeil et al., 2022).

Between 10-8 ka BP, the shoreline migrated to a geometry similar to present day and the growth rate of the Holocene reef and *Halimeda* bioherms domains reached their maximum values of 130.5 and 11.2 Gt/ka at 8.2 and 8.8 ka BP, respectively (Fig. 7b). Concurrently, much of the shelf edge reef had attained its maximum thickness and stopped accreting, therefore, its contribution to the sediment budget was gradually surpassed by the Holocene reef (Fig. 7c). RSL continued to rise until 4.8 ka BP with the maximum magnitude of the Mid-Holocene highstand (3.2 m) being predicted near Rockhampton and Mackay (Fig. 5) where the shoreline is estimated to have been up to tens of kilometres inland of its modern position, with the subsequent re-advance being due to the impact of water loading on the adjacent wide continental shelf. The growth rate of carbonate sediment decreased in the late Holocene, with the largest reduction seen in the Holocene

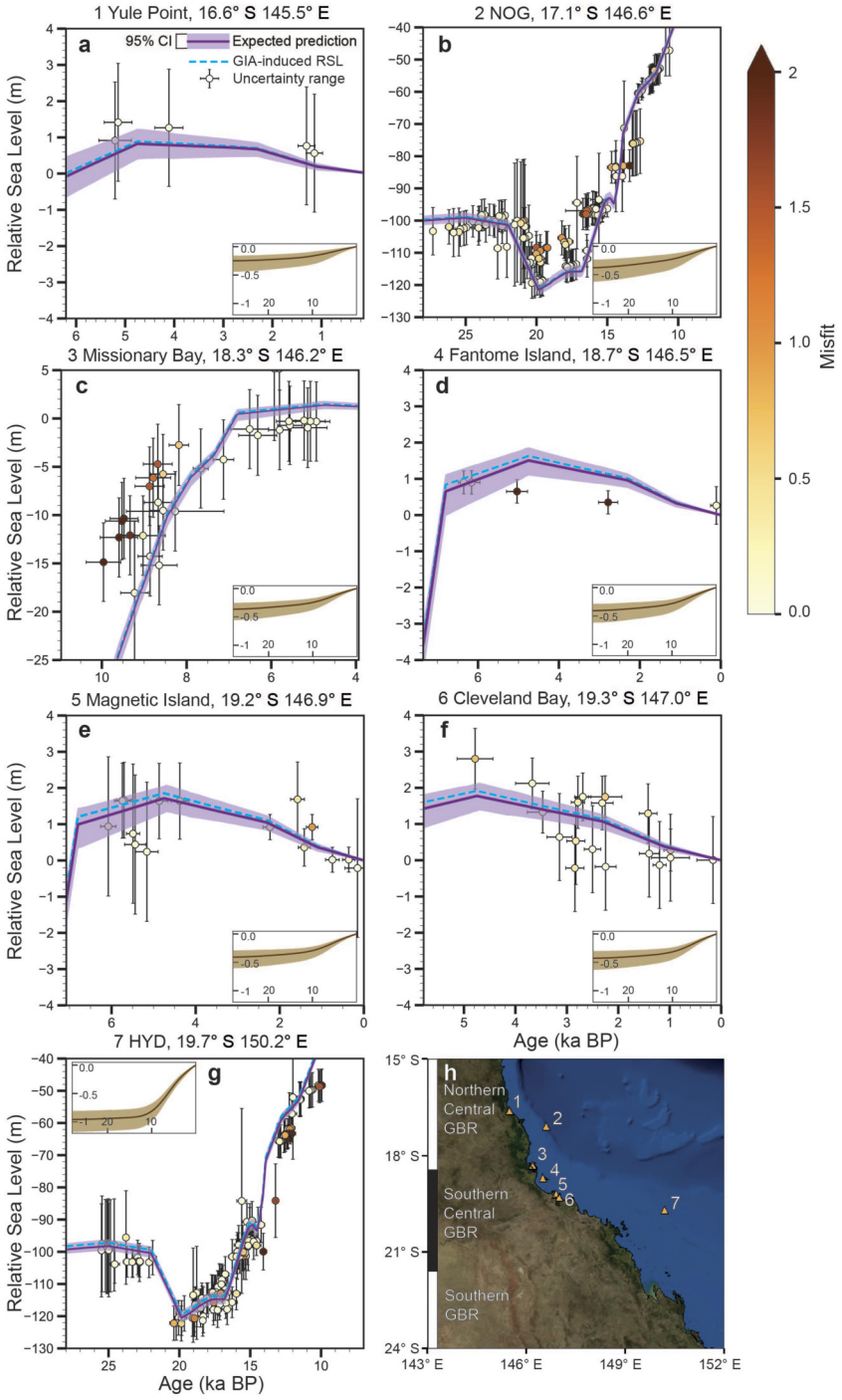

Fig. 4. Relative sea level data-model comparison. Each error bar shows 2σ vertical and age uncertainties with the coloured dots indicating the unitless data-model misfit (i.e., J in equation (5)). Note we plot the 2σ vertical uncertainty range of the reconstructed RSL instead of showing the original recorded elevation. The RSL sites are listed from north to south with the site's number, name and coordinates given as the subtitle. The expected SIA-induced RSL change and its associated 95% CI are shown in the subplot within each frame. The last frame shows the RSL site locations and corresponding site numbers. Note the different axes used in each plot.

reef domain due to the reef surface leaving the photic zone or the cessation of growth following the highstand (section 2.3.2). Overall, reconstructed Holocene growth rates for carbonate sediment domains agree well with the theoretical bell-shaped curve (Davies and Hopley, 1983), which suggests a slow growth during reef initiation followed by accelerated growth when the reef is "keeping-up" or "catching-up" to sea level. The final maturation phase exhibits a slow accretion rate mostly due to lack of accommodation space.

Our inversion results indicate the GBR experienced 1853.7 Gt (1613.1-2078.7 Gt) of sediment loading from MIS 2 to present (Fig. 7a). Three carbonate domains produced 1319.7 Gt (1007.5-1563.8 Gt) of sediment, comparable with previous estimates of 939 Gt (622-1398 Gt Hinestrosa et al., 2022) and 1709.4 Gt (Rees, 2005). The timing of increased carbonate deposition identified in our study correlates with a period of minor decrease in atmospheric CO_2 (14.3-12.7 ka BP), which is consistent with the idea that coral reef growth played a significant role in the postglacial

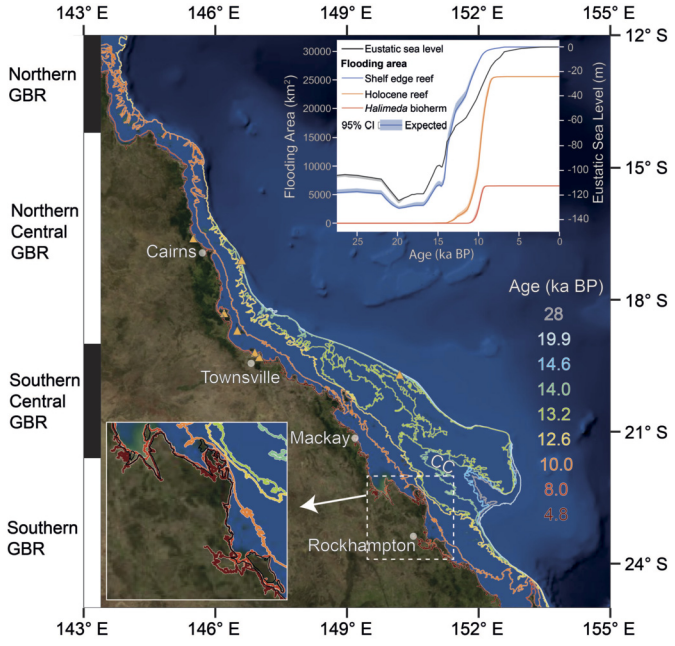

Fig. 5. Expected GBR postglacial flooding pattern. The eight coloured shoreline reconstructions correspond to the eight time intervals shown on the right. Time series of posterior flooding area for each sediment domain and eustatic sea-level are shown in the subplot in the top-right corner. The subplot in the bottom-left corner shows an enlarged version of the shoreline reconstruction results near Rockhampton. The orange triangles indicate site locations for the sea-level data shown in Fig. 4. Some key locations are labelled, CC = Capricorn Channel.

carbon cycle (Lemieux-Dudon et al., 2010; Kinsey and Hopley, 1991).

3.2.2. Spatial distribution

Fig. 7 shows the sediment spatial distribution conditioned on the SLIP database. There is a distinct north-south gradient with more sediment accumulated in the southern (central) GBR. This gradient reflects the different physiography of the northern and southern GBR, with the southern GBR having a wider and flatter shelf morphology. This provides ample accommodation space for carbonate material to grow (Fig. 3). The SLIPs support this gradient and mostly show higher-than-predicted RSL in the northern (central) GBR and, conversely, lower-than-predicted RSL in the southern central GBR. During sea-level transgression, the GBR sediment system is mostly in a depositional phase, therefore the effect of SIA is to increase the magnitude of post-depositional RSL rise, which results in lower-than-predicted RSL (Fig. 4). To minimise the misfit to SLIPs, model parameters associated with sediment domains in the northern (central) GBR gradually converged to the lower end of the prior distribution, producing 167.8 Gt and 229.8 Gt of sediment. In contrast, the southern central GBR sediment mass distributions strongly skew to the higher end, producing 994.6 Gt of sediment. Although there are no SLIPs in the southern GBR sector, the larger-than-prior sediment loading results (461.5 Gt) reflect the fact that sediment loading in the southern sector has a long-wavelength impact on RSL change in the southern central GBR.

This north-south distinction is supported by recent seismic mapping of shelf edge reef structures (Hinestrosa et al., 2016, 2014) and a modelling study of the GBR carbonate-siliciclastic systems (Salles et al., 2018), both of which show substantially thicker shelf edge sediment in the southern (central) GBR. The good agreement between RSL observations and these independent studies suggests it is possible to use SLIPs to constrain sediment deposition history. It is noticeable that, compared with other regions, the posterior uncertainties are very low in the southern central GBR (Fig. 7b). The reason for this is because greater southern central sediment loading consistently improves the data-model misfit, by up to ~15%, and thus the southern central sediment loading converges to the higher end of the prior distribution. For the other three regions, because the overall misfits are sensitive to the southern-central load, they show a similar level of uncertainty.

3.2.3. SIA-induced RSL change

Using the posterior model parameter distributions, we quantify the impact of SIA on the total GBR RSL calculation (Fig. 4). Overall, including the SIA signal reduces the data-model misfit (J in equation (4)) by ~10% and broadens the acceptable region of the Earth model parameter space (Supplementary Figure 7). The largest SIA signal is on the outer shelf of the southern-central GBR where sediment loading contributes >1.1 m to RSL rise since MIS 2 (Fig. 7c). For HYD, incorporating the SIA-induced RSL rise (0.97 m; 0.83-1.17 m) improves the model fit to the SLIPs from 0.48 to 0.41, especially for SLIPs with ages 12.5-10 and 21-18 ka BP where observations show remarkably lower RSL than predicted by the GIA-only model. For the inner shelf region of the southern-central GBR, the SIA signal is lower, with an expected value of only 0.42 m (0.31-0.64 m; similar magnitude for sites 4-6), due to the lack of carbonate sediment. Similar to HYD, the inclusion of the SIA signal significantly improves the average model misfit by 0.04 for Fantome Island. But for Magnetic Island and Cleveland Bay, there is no noticeable improvement. For these four RSL sites, since the majority of sediment loading takes place at the shelf edge and in the Holocene reef domains, i.e., during the early-mid Holocene, the SIA signal remains almost unchanged before 14 ka BP (Fig. 4).

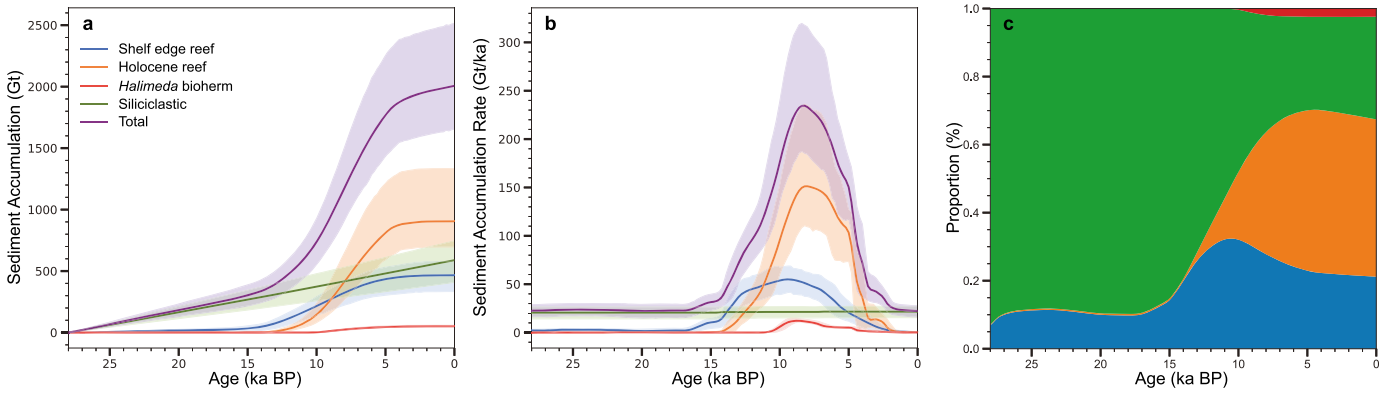

Fig. 6. GBR posterior sediment mass accumulation history. (a) Total sediment mass accumulation and sediment accumulation associated with each sediment domain. (b) As in (a), but showing the rate of sediment accumulation. The solid lines indicate the expected sediment models and uncertainty ranges denote the 95% confidence intervals. (c) The proportional contribution of each sediment domain to total mass accumulation through time.

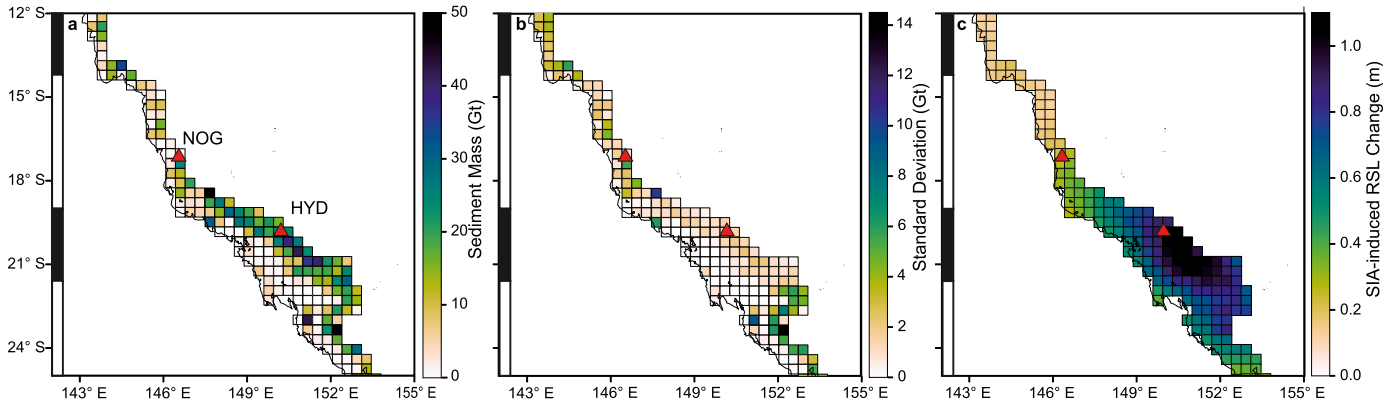

Fig. 7. Reconstructed spatial distribution of sediment mass accumulated from MIS 2 to present. (a) Expected sediment accumulation mass distribution. (b) One sigma standard deviation of sediment accumulation mass. (c) Expected RSL change due to SIA. The black and white bands on the left define the four GBR latitudinal sectors as in Fig. 5. The red triangles indicate the locations of NOG and HYD.

To the north, SIA effects in Missionary Bay and Noggin Pass are predicted to have a similar magnitude of ~0.3 m, but with different temporal patterns (Fig. 4). For Missionary Bay, the local load is minor (<10 Gt; Fig. 7a) and the SIA signal is primarily impacted by the long wavelength sediment signal from the southern-central GBR, where 910.7 Gt of sediment was deposited during the Holocene. In contrast, the SIA signal for NOG shows a much more linear rate of prior to before the Holocene, which is caused by continuous siliciclastic sediment discharge to the shelf edge during early deglaciation. Lastly, for Yule Point the SIA signal is predicted to be small (0.24 m) due to the low local sediment loading and the fact that it is located >500 km from the sediment deposition centre in the southern central GBR. Since the SLIPs generally show higher-than-predicted RSL at sites 1-3, the inclusion of the SIA signal slightly increases the model misfit to observations. But since the SIA signals for these sites are relatively small, the overall increase in model misfit is negligible compared with the misfit reduction associated with including SIA in the southern central GBR.

4. Discussion

4.1. GBR RSL spatial variability

We first investigate the degree to which the SIA signal can explain the RSL difference between NOG and HYD. The Monte Carlo binning analysis (section 2.4.1) yields a temporally-increasing RSL difference between these two locations, with a temporally-averaged value of 4.0 m (3.4-4.5 m, Fig. 8). The increasing RSL difference at NOG and HYD prior to the Holocene can be explained by different sediment deposition histories. Between MIS 2 and the Holocene a considerable amount of siliciclastic sediment was discharged to the shelf edge near NOG, which gradually increased local RSL (Fig. 4). Comparatively, our model predicts much less siliciclastic discharge near HYD (this site is not located close to any modern river mouths, Fig. 3), hence the SIA signal remains low prior to the Holocene. These results are consistent with conceptual sediment depositional models which suggest that, during MIS 2 and MIS 1, the regions surrounding NOG and HYD were dominated by large estuaries and extensive coastal barriers and lagoons (Hinestrosa et al., 2016). Near NOG, the estuaries were fed by east-west elongated channels crossing the narrow continental shelf (<50 km) which provided an efficient way to transport coarse grained sediment to the shelf edge and upper continental slope. This can be verified by the presence of thick siliciclastic sediment in various records from the shelf edge and continental slope (Dunbar and Dickens, 2003). In contrast, the northwest-southeast elongated coastal choked lagoons of the southern central GBR were not efficient for transporting sediment towards the continental slope. The wider and flatter continental shelf in this region nurtured complex drainage networks with long and sinuous channels redirecting the sediment to the southeast (see Figure 1 of Hinestrosa et al., 2016). In addition, the presence of blocking barriers along the shelf edge strongly reduced lagoon flushing. In summary, prior to coral reef initiation during the Holocene, NOG was substantially more impacted by siliciclastic sediment loading than HYD (Fig. 4), which explains the greater RSL rise observed at NOG during this period.

Subsequent to the initiation of reef development, HYD has experienced greater RSL rise than NOG, due to the development of extensive reefs in the southern central GBR. Specifically, our sediment model predicts the development of widespread, thick reefs across the shelf edge of the southern central, resulting in up to four times more sediment loading compared with the northern central GBR. This is consistent with seismic stratigraphy suggesting the extensive availability of low gradient substrate near HYD promoted the development of thick and wide fringing shelf edge reefs (Hinestrosa et al., 2016). In comparison, the lateral availability of substrate is very limited near NOG due to the narrow and steep physiography (Abbey et al., 2011). Additionally, our results show shelf edge reefs near HYD are thicker than those near NOG, consistent with the drill core observations shown in Supplementary Figure 1. This may be due to the contrasting palaeo-environmental and physiographic conditions between NOG and HYD during the evolution of these reefs (e.g., different morphology and sediment and nutrient circulation; Hinestrosa et al., 2016). Similar to the shelf edge reef, a wide and flat physiography provides ample accommodation space for the Holocene reef to thrive in southern central GBR. Our interpolation results suggest the Holocene reef in this region is on average thicker than in the north (Supplementary section 1) possibly due to the lower elevation prior to sea-level transgression (Salles et al., 2018; Hopley et al., 2007). Overall, based on our expected sediment and Earth model parameters, we predict that sediment loading differences between NOG and HYD can explain 0.6 m (0.35-0.75 m) of the observed RSL difference.

Notably, our SIA model can only account for 15% of the mean RSL difference (4.0 m) between NOG and HYD. We propose three possible explanations for this. Firstly, as mentioned in section 3.1, our preferred Earth models are relatively strong (Table 2). These Earth models may be biased towards fitting LGM-age SLIPs from NOG and HYD, but it is important to note that these SLIPs have large chronological and indicative meaning uncertainties. Previous GIA analysis (e.g., Lambeck et al., 2002) and independent 3D mantle viscosity estimates suggest a thinner lithosphere and weaker

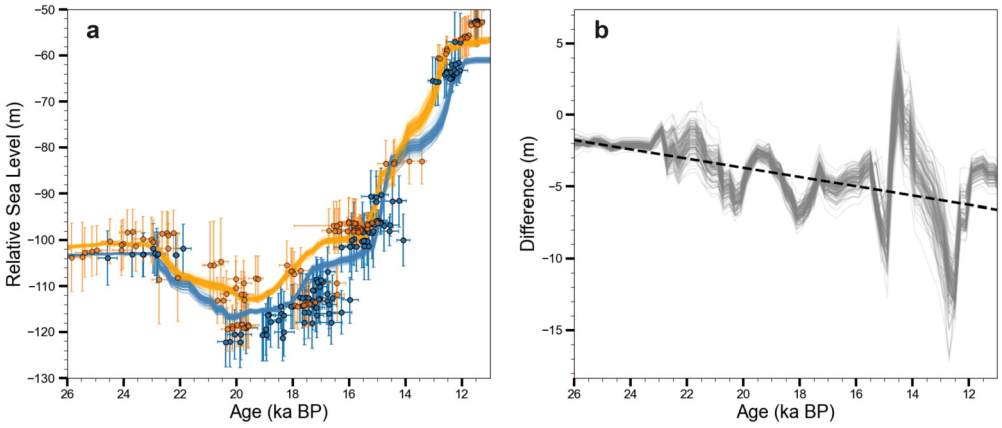

Fig. 8. Monte Carlo binning analysis results. (a) Reconstructed time series of RSL variation at NOG (orange) and HYD (blue). The error bars indicate 2σ age and vertical data uncertainties. Each solid line represents one random realisation of the Monte Carlo binning analysis. (b) The time series of RSL difference between NOG and HYD, the dashed trendline indicates the temporally increasing RSL difference between these two sites from the LGM to the Holocene.

mantle viscosity across the GBR, which would induce a larger SIA signal and explain more of the RSL difference between NOG and HYD. Therefore, we recalculate the SIA signal using an alternative Earth model with 46 km lithospheric thickness and 0.1×10^{21} Pa s upper mantle viscosity, which is supported by previous studies (Hoggard et al., 2021; Austermann et al., 2021) and is consistent with the Earth model determined by the Holocene SLIPs alone (Supplementary Figure 6). The results show a larger SIA signal at NOG (0.59 m) and HYD (2.20 m), which accounts for almost half the observed RSL difference.

Secondly, differences in turbidity and nutrient level may impact the coral species' living depth and hence past RSL reconstructions (Hibbert et al., 2016). One important assumption when reconstructing past sea level is that each sea-level indicator of a given species should have an identical relationship to palaeo water depth, however, this is not robust. Indeed, there is no global relationship between coral species and bathymetry (Perrin et al., 1995), instead, it depends on local irradiance levels (affected by turbidity and nutrient levels), nutrient availability, temperature and hydrodynamic conditions (Hibbert et al., 2016). As mentioned above, NOG and HYD are dominated by estuarine and lagoonal environments, this difference may induce significantly different coral reef accretion environments, which could explain part of the observed RSL difference between NOG and HYD (Hinestrosa et al., 2016).

Thirdly, the simple sediment model adopted in this study may not adequately represent sediment evolution across the GBR, especially the terrigenous sediment transport and depositional processes. Although the impact of shoreline migration is considered, we do not account for landscape and fluvial evolution driven by extrinsic forcings and sea-level variation or the sediment infill of some large palaeo river channels (Ryan et al., 2007), and instead we make the simple assumption that fluvial sediment is deposited (with an overall uniform rate) at the nearest concurrent shoreline position. These factors may misrepresent the spatio-temporal distribution of siliciclastic sediment. For example, our siliciclastic modelling results are similar to a classical reciprocal sedimentation concept, which may not fit well with the deglacial sediment accumulation rate inferred from sediment cores from Queensland Trough (Dunbar et al., 2000). Additionally, we do not consider the effect of wave processes on siliciclastic sedimentation, which can induce erosional and depositional phases near NOG and HYD (see Figure 4 of Salles et al., 2018).

Lastly, we note acknowledge that the relatively coarse resolution of the sediment SIA model used in this study may cannot be able to fully resolve coral reef structure (Fig. 7), which is often characterised by narrow and isolated strips with <1 km coverage (Hinestrosa et al., 2016). This caveat and this may lead to structural bias in the resulting SIA signal. Rovere et al. (2022, preprint) provide a direct comparison of the SIA signals estimated by SIA models with 1 km and 40 km resolution (see their Figure 4b and 4f). Their results indicate although both SIA models produce a long wavelength SIA signal, the low-resolution SIA model would systematically underpredict SIA signal, especially in regions with non-continuous sediment load. Therefore, this potential for our model to underestimate the local SIA signal may further explain some of the RSL difference between NOG and HYD. Considering all of the factors discussed here, we conclude that it is possible for the SIA process to partially explain the observed spatial variability in RSL between NOG and HYD. However, to better understand this RSL variability, further investigation is required of the missing processes mentioned above.

4.2. SIA impact on ice volume estimate

Using far-field sea-level data to constrain past grounded ice volume and infer past ice sheet dynamics is an important tool in palaeoclimate studies (e.g., Lambeck et al., 2014). However, most studies do not consider the SIA signal, despite previous studies suggesting it can alter local RSL by >100 m since the Last Interglacial (Pico, 2020). Because SIA-induced RSL change is not associated with ice-water exchange, neglecting its effect will systematically bias inferences of global grounded ice volume. For the GBR, we find that SIA can cause up to 1.1 m RSL rise since MIS 2, which is equivalent to overestimating the volume of ice melt by $\sim 4.3 \times 10^5$ km^3 under the common assumption that ice-water exchange is the only cause of post-glacial sea-level change. This demonstrates that caution is needed when estimating global ice volume from SLIPs collected from margins characterised by high sediment input across large spatial areas (hundreds of kilometres, e.g., Argentine Shelf).

Based on the results of this study, we find that it is necessary to incorporate the SIA signal when determining global ice volume during the LGM, which is an outstanding problem in paleoclimate studies (Simms et al., 2019). Currently, there are five locations that have yielded RSL records for the LGM, specifically, NOG, HYD, Bonaparte Gulf, Sunda Shelf and Barbados. All of these locations are potentially impacted by sediment loading during the last deglaciation. In particular, cores from NOG, HYD and Barbados were collected from large coral reef frameworks near estuaries (Woodroffe and Webster, 2014) which are likely to have been affected by RSL rise due to reef and siliciclastic sediment loading. Although distant from large coral reef systems, Bonaparte Gulf and Sunda Shelf are located near major river mouths (Pico, 2020), and

they may record some SIA signals caused by siliciclastic sediment deposition. In all cases, incorporating the SIA process will reduce the subsequent global grounded ice volume estimate, which will help to mitigate the current disagreement between the magnitude of post-LGM GMSL rise recorded by RSL indicators and the estimated amount of ice melt (Simms et al., 2019).

5. Conclusions

In this study, we develop a systematic RSL-driven framework to reconstruct a sediment deposition history for the world's largest carbonate-siliciclastic sediment system, the GBR. Using a Bayesian-style technique, we calibrate the sediment history along with SIA- and GIA-induced RSL change using SLIPs from the GBR region. Based on our results, we highlight these key findings:

1. From MIS 2 to present, 1853.7 Gt (1613.1-2078.7 Gt) of sediment were deposited along the GBR consisting of 1319.7 Gt (1007.5-1563.8 Gt) of carbonate sediment, which mostly accreted between the late Pleistocene and mid Holocene, and 534.0 Gt (410.5-659.1 Gt) of terrigenous siliciclastic sediment.
2. There is a strong north-south gradient in the reconstructed sediment loading, with ∼75% of the sediment predicted to have been deposited in the southern-central and southern GBR. This latitudinal distinction is consistent with independent seismic stratigraphy analysis (Hinestrosa et al., 2014), continental shelf physiography (Hinestrosa et al., 2016) and sea-level observations (Yokoyama et al., 2018; Webster et al., 2018).
3. For the GBR, SIA can contribute up to 1.1 m of RSL rise during the last deglaciation. Neglecting its contribution to RSL will lead to an $\sim 4.3 \times 10^5$ km^3 overestimate of global grounded ice volume during the LGM. To accurately infer global ice volume from far-field SLIPs, we suggest a systematic assessment of the potential SIA signal is required, especially for SLIP locations near large sediment systems.

CRediT authorship contribution statement

Y.L. led the research; Y.L., P.L.W., F.D.H. and S.A.W. conceived the scope and design of the research. Y.L., P.L.W., F.D.H. and S.A.W. led the writing of the manuscript. G.H. and J.M.W. guided Y.L. in building the sediment model. P.L.W. advised Y.L. in performing GIA and SIA modelling. F.D.H., S.A.W., G.H. and J.M.W. advised Y.L. in sediment data analysis. All authors contributed ideas and to the writing of the manuscript.

Declaration of competing interest

The authors declare that they have no known competing financial interests or personal relationships that could have appeared to influence the work reported in this paper.

Data availability

The relative sea-level data used for this study along with the reconstructed sediment deposition, and relative sea-level change history and shoreline migration patterns across the Great Barrier Reef, and the SIA emulator are available at https://github.com/yc-lin-geo/GBR-Sediment. The code for generating the depth uncertainty distribution for each type of sea-level indicator can be accessed from Hibbert et al. (2018), via https://figshare.com/articles/dataset/Matlab_Code_-_calculation_of_sea_level/5890579.

Acknowledgements

The authors thank two anonymous reviewers for their constructive comments, and Glenn A. Milne for providing the code used to perform the GIA modelling. Y.L. was supported by a China Scholarship Council - Durham University joint scholarship (No. 201908190020). F.D.H. received funding from the European Union's Horizon 2020 research and innovation programme under the Marie Skłodowska-Curie grant agreement (No. 838841 – ExTaSea). J.M.W. received funding from the Australian Research Council (DP1094001). The authors acknowledge the collaborative research oppurtunities created by PALSEA, a working group of the International Union for Quaternary Sciences (INQUA) and Past Global Changes (PAGES), which in turn received support from the Swiss Academy of Sciences and the Chinese Academy of Sciences.

Appendix A. Supplementary material

Supplementary material related to this article can be found online at https://doi.org/10.1016/j.epsl.2023.118066.

References

Abbey, Elizabeth, Webster, Jody M., Beaman, Robin J., 2011. Geomorphology of submerged reefs on the shelf edge of the Great Barrier Reef: the influence of oscillating Pleistocene sea-levels. Mar. Geol. 288 (1–4), 61–78.
Austermann, Jacqueline, Hoggard, Mark J., Latychev, Konstantin, Richards, Fred D., Mitrovica, Jerry X., 2021. The effect of lateral variations in Earth structure on Last Interglacial sea level. Geophys. J. Int. 227 (3), 1938–1960.
Beaman, R.J., 2010. 3DGBR: a high-resolution depth model for the Great Barrier Reef and Coral Sea. In: Marine and Tropical Sciences Facility (MTSRF) Project, 2, p. 13.
Cheng, Hai, Edwards, R. Lawrence, Shen, Chuan-Chou, Polyak, Victor J., Asmerom, Yemane, Woodhead, Jon, Hellstrom, John, Wang, Yongjin, Kong, Xinggong, Spötl, Christoph, et al., 2013. Improvements in 230Th dating, 230Th and 234U half-life values, and U–Th isotopic measurements by multi-collector inductively coupled plasma mass spectrometry. Earth Planet. Sci. Lett. 371, 82–91.
Dalca, A.V., Ferrier, K.L., Mitrovica, J.X., Perron, J.T., Milne, G.A., Creveling, J.R., 2013. On postglacial sea level—III. Incorporating sediment redistribution. Geophys. J. Int. 194 (1), 45–60.
Davies, Peter J., Hopley, David, 1983. Growth fabrics and growth rates of Holocene reefs in the Great Barrier Reef. BMR J. Aust. Geol. Geophys. 8, 237–251.
Dunbar, Gavin B., Dickens, Gerald R., 2003. Massive siliciclastic discharge to slopes of the Great Barrier Reef Platform during sea-level transgression: constraints from sediment cores between 15 S and 16 S latitude and possible explanations. Sediment. Geol. 162 (1–2), 141–158.
Dunbar, G.B., Dickens, G.R., Carter, R.M., 2000. Sediment flux across the Great Barrier Reef Shelf to the Queensland Trough over the last 300 ky. Sediment. Geol. 133 (1–2), 49–92.
Dziewonski, Adam M., Anderson, Don L., 1981. Preliminary reference Earth model. Phys. Earth Planet. Inter. 25 (4), 297–356.
Ferrier, Ken L., Austermann, Jacqueline, Mitrovica, Jerry X., Pico, Tamara, 2017. Incorporating sediment compaction into a gravitationally self-consistent model for ice age sea-level change. Geophys. J. Int. 211 (1), 663–672.
Ferrier, Ken L., Li, Qi, Pico, Tamara, Austermann, Jacqueline, 2018. The influence of water storage in marine sediment on sea-level change. Geophys. Res. Lett. 45 (5), 2444–2454.
Heaton, Timothy J., Köhler, Peter, Butzin, Martin, Bard, Edouard, Reimer, Ron W., Austin, William E.N., Bronk Ramsey, Christopher, Grootes, Pieter M., Hughen, Konrad A., Kromer, Bernd, et al., 2020. Marine20—the marine radiocarbon age calibration curve (0–55, 000 cal BP). Radiocarbon 62 (4), 779–820.
Hibbert, Fiona D., Rohling, Eelco J., Dutton, Andrea, Williams, Felicity H., Chutcharavan, Peter M., Zhao, Cheng, Tamisiea, Mark E., 2016. Coral indicators of past sea-level change: a global repository of U-series dated benchmarks. Quat. Sci. Rev. 145, 1–56.
Hibbert, F.D., Williams, F.H., Fallon, S.J., Rohling, E.J., 2018. A database of biological and geomorphological sea-level markers from the Last Glacial Maximum to present. Sci. Data 5, 180088.
Hinestrosa, Gustavo, Webster, Jody M., Beaman, Robin J., Anderson, Louise M., 2014. Seismic stratigraphy and development of the shelf-edge reefs of the Great Barrier Reef, Australia. Mar. Geol. 353, 1–20.
Hinestrosa, Gustavo, Webster, Jody M., Beaman, Robin J., 2016. Postglacial sediment deposition along a mixed carbonate-siliciclastic margin: new constraints from the drowned shelf-edge reefs of the Great Barrier Reef, Australia. Palaeogeogr. Palaeoclimatol. Palaeoecol. 446, 168–185.

Hinestrosa, Gustavo, Webster, Jody M., Beaman, Robin J., 2019. Spatio-temporal patterns in the postglacial flooding of the Great Barrier Reef shelf, Australia. Cont. Shelf Res. 173, 13–26.
Hinestrosa, Gustavo, Webster, Jody M., Beaman, Robin J., 2022. New constraints on the postglacial shallow-water carbonate accumulation in the Great Barrier Reef. Sci. Rep. 12 (1), 1–18.
Hogg, Alan G., Heaton, Timothy J., Hua, Quan, Palmer, Jonathan G., Turney, Chris S.M., Southon, John, Bayliss, Alex, Blackwell, Paul G., Boswijk, Gretel, Bronk Ramsey, Christopher, et al., 2020. SHCal20 Southern Hemisphere calibration, 0–55,000 years cal Bp. Radiocarbon 62 (4), 759–778.
Hoggard, Mark, Austermann, Jacqueline, Randel, Cody, Stephenson, Simon, 2021. Observational estimates of dynamic topography through space and time. Mantle Convect. Surf. Expr., 371–411.
Hopley, David, Smithers, Scott G., Parnell, Kevin, 2007. The Geomorphology of the Great Barrier Reef: Development, Diversity and Change. Cambridge University Press.
Horton, Benjamin P., Kopp, Robert E., Garner, Andra J., Hay, Carling C., Khan, Nicole S., Roy, Keven, Shaw, Timothy A., 2018. Mapping sea-level change in time, space, and probability. Annu. Rev. Environ. Resour. 43, 481–521.
Ishiwa, Takeshige, Yokoyama, Yusuke, Okuno, Jun'ichi, Obrochta, Stephen, Uehara, Katsuto, Ikehara, Minoru, Miyairi, Yosuke, 2019. A sea-level plateau preceding the Marine Isotope Stage 2 minima revealed by Australian sediments. Sci. Rep. 9 (1), 1–8.
Ji, Weiwen, Robel, Alexander, Tziperman, Eli, Yang, Jun, 2021. Laurentide ice saddle mergers drive rapid sea level drops during glaciations. Geophys. Res. Lett. 48 (14), e2021GL094263.
Kendall, Roblyn A., Mitrovica, Jerry X., Milne, Glenn A., 2005. On post-glacial sea level–II. Numerical formulation and comparative results on spherically symmetric models. Geophys. J. Int. 161 (3), 679–706.
Kinsey, D.W., Hopley, D., 1991. The significance of coral reefs as global carbon sinks—response to greenhouse. Palaeogeogr. Palaeoclimatol. Palaeoecol. 89 (4), 363–377.
Kirkpatrick, Scott, Gelatt, C. Daniel, Vecchi, Mario P., 1983. Optimization by simulated annealing. Science 220 (4598), 671–680.
Lambeck, Kurt, Yokoyama, Yusuke, Purcell, Tony, 2002. Into and out of the Last Glacial Maximum: sea-level change during Oxygen Isotope Stages 3 and 2. Quat. Sci. Rev. 21 (1–3), 343–360.
Lambeck, Kurt, Rouby, Hélène, Purcell, Anthony, Sun, Yiying, Sambridge, Malcolm, 2014. Sea level and global ice volumes from the Last Glacial Maximum to the Holocene. Proc. Natl. Acad. Sci. 111 (43), 15296–15303.
Lemieux-Dudon, Bénédicte, Blayo, Eric, Petit, Jean-Robert, Waelbroeck, Claire, Svensson, Anders, Ritz, Catherine, Barnola, Jean-Marc, Narcisi, Bianca Maria, Parrenin, Frédéric, 2010. Consistent dating for Antarctic and Greenland ice cores. Quat. Sci. Rev. 29 (1–2), 8–20.
Lin, Yucheng, 2019. Closing the Last Deglacial Global Sea Level Budget by Different Antarctic Deglaciation Models. Masters dissertation. The Australian National University, Canberra.
Lin, Yucheng, Hibbert, Fiona D., Whitehouse, Pippa L., Woodroffe, Sarah A., Purcell, Anthony, Shennan, Ian, Bradley, Sarah L., 2021. A reconciled solution of Meltwater Pulse 1A sources using sea-level fingerprinting. Nat. Commun. 12 (1), 1–11.
Love, Ryan, Milne, Glenn A., Tarasov, Lev, Engelhart, Simon E., Hijma, Marc P., Latychev, Konstantin, Horton, Benjamin P., Törnqvist, Torbjörn E., 2016. The contribution of glacial isostatic adjustment to projections of sea-level change along the Atlantic and Gulf coasts of North America. Earth's Future 4 (10), 440–464.
McNeil, Mardi A., Webster, Jody M., Beaman, Robin J., Graham, Trevor L., 2016. New constraints on the spatial distribution and morphology of the Halimeda bioherms of the Great Barrier Reef, Australia. Coral Reefs 35 (4), 1343–1355.
McNeil, Mardi A., Nothdurft, Luke D., Dyriw, Nicholas J., Webster, Jody M., Beaman, Robin J., 2020. Morphotype differentiation in the Great Barrier Reef Halimeda bioherm carbonate factory: internal architecture and surface geomorphometrics. Depositional Rec. 7 (2), 176–199.
McNeil, Mardi, Nothdurft, Luke D., Hua, Quan, Webster, Jody M., Moss, Patrick, 2022. Evolution of the inter-reef Halimeda carbonate factory in response to Holocene sea-level and environmental change in the Great Barrier Reef. Quat. Sci. Rev. 277, 107347.
Milliman, John D., Farnsworth, Katherine L., 2013. River Discharge to the Coastal Ocean: A Global Synthesis. Cambridge University Press.
Mitrovica, Jerry X., Wahr, John, Matsuyama, Isamu, Paulson, Archie, 2005. The rotational stability of an ice-age Earth. Geophys. J. Int. 161 (2), 491–506.
Perrin, Christine, Bosence, Dan, Rosen, Brian, 1995. Quantitative approaches to palaeozonation and palaeobathymetry of corals and coralline algae in Cenozoic reefs. Geol. Soc. (Lond.) Spec. Publ. 83 (1), 181–229.
Pico, T., 2020. Towards assessing the influence of sediment loading on Last Interglacial sea level. Geophys. J. Int. 220 (1), 384–392.
Rees, Siwan Angharad, 2005. Coral reefs of the Indo-Pacific and changes in global Holocene. PhD thesis. University of Southampton.
Rovere, Alessio, Pico, Tamara, Richards, Fred D., O'Leary, Michael J., Mitrovica, Jerry X., Goodwin, Ian D., Austermann, Jacqueline, Latychev, Konstantin, 2022. The influence of reef isostasy, dynamic topography, and glacial isostatic adjustment on the Last Interglacial sea-level record of Northeastern Australia. https://doi.org/10.31223/X55S8X.
Ryan, David A., Bostock, Helen C., Brooke, Brendan P., Marshall, John F., 2007. Bathymetric expression of the Fitzroy River palaeochannel, northeast Australia: response of a major river to sea-level change on a semi-rimmed, mixed siliciclastic-carbonate shelf. Sediment. Geol. 201 (1–2), 196–211.
Salles, Tristan, Ding, Xuesong, Webster, Jody M., Vila-Concejo, Ana, Brocard, Gilles, Pall, Jodie, 2018. A unified framework for modelling sediment fate from source to sink and its interactions with reef systems over geological times. Sci. Rep. 8 (1), 1–11.
Sanborn, Kelsey L., Webster, Jody M., Webb, Gregory E., Carlos Braga, Juan, Humblet, Marc, Nothdurft, Luke, Patterson, Madhavi A., Dechnik, Belinda, Warner, Susan, Graham, Trevor, et al., 2020. A new model of Holocene reef initiation and growth in response to sea-level rise on the Southern Great Barrier Reef. Sediment. Geol. 397, 105556.
Simms, Alexander R., Lisiecki, Lorraine, Gebbie, Geoffrey, Whitehouse, Pippa L., Clark, Jordan F., 2019. Balancing the last glacial maximum (LGM) sea-level budget. Quat. Sci. Rev. 205, 143–153.
Tarasov, Lev, Dyke, Arthur S., Neal, Radford M., Peltier, W. Richard, 2012. A data-calibrated distribution of deglacial chronologies for the North American ice complex from glaciological modeling. Earth Planet. Sci. Lett. 315, 30–40.
Webster, Jody M., Carlos Braga, Juan, Humblet, Marc, Potts, Donald C., Iryu, Yasufumi, Yokoyama, Yusuke, Fujita, Kazuhiko, Bourillot, Raphael, Esat, Tezer M., Fallon, Stewart, et al., 2018. Response of the Great Barrier Reef to sea-level and environmental changes over the past 30,000 years. Nat. Geosci. 11 (6), 426.
Wolstencroft, Martin, Shen, Zhixiong, Törnqvist, Torbjörn E., Milne, Glenn A., Kulp, Mark, 2014. Understanding subsidence in the Mississippi Delta region due to sediment, ice, and ocean loading: insights from geophysical modeling. J. Geophys. Res., Solid Earth 119 (4), 3838–3856.
Woodroffe, Colin D., Webster, Jody M., 2014. Coral reefs and sea-level change. Mar. Geol. 352, 248–267.
Yokoyama, Yusuke, Purcell, Anthony, Marshall, John F., Lambeck, Kurt, 2006. Sea-level during the early deglaciation period in the Great Barrier Reef, Australia. Glob. Planet. Change 53 (1–2), 147–153.
Yokoyama, Yusuke, Esat, Tezer M., Thompson, William G., Thomas, Alexander L., Webster, Jody M., Miyairi, Yosuke, Sawada, Chikako, Aze, Takahiro, Matsuzaki, Hiroyuki, Okuno, Jun'ichi, et al., 2018. Rapid glaciation and a two-step sea level plunge into the Last Glacial Maximum. Nature 559 (7715), 603–607.